



3D-printed, ceramic porous metasurface wick: Hexagonal-prism unit-cell capillary evaporator

Lorenzo Franceschetti^a, Yuki Kameya^b, Massoud Kaviany^{a,*}

^a Department of Mechanical Engineering, University of Michigan, Ann Arbor, MI, 48109, United States

^b Department of Mechanical Engineering, Chiba Institute of Technology, Narashino, Japan

ARTICLE INFO

Keywords:

Surface Evolver
Receding meniscus
Open-system evaporator
Alumina (ceramic) wick

ABSTRACT

A hexagonal-prism unit-cell based alumina evaporator wick with 150 μm struts and 375 μm wick thickness is designed and fabricated with 3D-printing using projection micro stereolithography and post debinding and sintering. The evaporator wick capillary pressure, permeability, effective thermal conductivity, and specific thermal conductance are calculated using static surface-energy minimization for the liquid meniscus-capillary pressure and 3-D CFD simulations. In comparison to a close-packed, sintered copper particle (average diameter of 78 μm) monolayer wick used in a similar, previous experiment, the ceramic wick has a much larger capillary-viscous critical heat flux $q_{CHF,c-v}$. However, the specific thermal conductance of the ceramic wick is about 1/10, due to its larger thickness and lower effective thermal conductivity, such that the wick superheat critical heat flux $q_{CHF,sh}$ controls the upper limit of its performance. The ceramic hexagonal-prism unit-cell wick outperforms this monolayer sintered-copper wick, when used for open-system evaporation. The experiment uses water and a 10 mm \times 20 mm partially submerged alumina wick with contact heating area of 8 mm \times 8 mm, under incremental increase in the heating rate up to the wick superheat limit. Infrared thermometry (with an estimate of the wet-wick surface emissivity) is used for the wick surface temperature. The 3-D numerical simulations show the fin effect in the lower, unheated wick section and the predictions, including the average wick-surface temperature, are in good agreement with the measurements.

1. Introduction

Metasurfaces are unit-cell based structures engineered for specific functions such as surface acoustics or electromagnetic wave behavior [1]. Porous metasurfaces have unit-cell pore structures designed for control of a surface behavior, for example, acoustic impedance or multiple-scattering features. Metasurfaces for controlled wettability include unique adaptive property advantages compared with traditionally engineered systems. Such surfaces involve changes in the surface chemistry or structure offered by additive manufacturing methods including two-photon lithography for high-resolution 3-D microstructures. A mechano-adaptive surface with strain-dependent wettability from hydrophobic to the super-hydrophobic has been introduced in [2]. In the field of two-phase flow and heat transfer, porous metasurfaces can be used to optimize capillarity and effective transport properties, for example, in the design of wicks used for liquid-vapor phase change heat transfer, i.e., evaporation [3,4].

Traditionally, high-performance porous evaporator wick metasurfaces have been fabricated by sintering metallic powders in a furnace. Applications based on these sintered metallic powder evaporating wicks

have included modulated wick enhanced pool boiling [5], modulated wick heat pipes (e.g., [6]), multiple-artery vapor chambers [7,8], and in the flow-boiling canopy wick [9]. In these applications, the local liquid arteries provide liquid to the evaporator (generally a monolayer wick for minimal thermal resistance) and this results in large dryout limits (so-called wick capillary viscous and superheat limits). Another application of the wicks are open-system metasurface evaporators which can be used in many thermal energy conversion devices, such as solar-driven steam production [10], with the goal of efficient liquid surface evaporation minimizing heat loss. Recently, sintered copper particle wicks with enhanced surface area (using arteries) have been explored for efficient, open-system water vapor generation [3].

In recent years, 3D-printing (additive manufacturing), rather than oven-sintering, of metallic evaporating wicks has been explored, particularly for heat pipe applications [11,12]. This 3D-printing has used metal powders to form solid structures, for example, structures of solid matrix (lattices also called cellular materials) with solid elements having a density near 100%. The authors of [13] used a photosensitive aluminum-alloy slurry-resin and stereolithography to form a

* Corresponding author.

E-mail address: kaviany@umich.edu (M. Kaviany).

Nomenclature**Roman Symbols**

A	Area, m ²
d	Diameter, m
G	Thermal conductance, W/K
g	Gravitational acceleration, m/s ²
Δh_{lg}	Heat of vaporization, J/kg
$\langle k \rangle$	Effective thermal conductivity, W/m-K
K	Permeability, m ²
k	Thermal conductivity, W/m-K
k_K	Kozeny coefficient
L	Length, m
\dot{M}	Mass flow rate, kg/s
\dot{m}	Mass flux, kg/m ² -s
M	Mass, kg
p	Pressure, Pa
q	Heat flux, W/m ²
ΔT_{sh}	Wick superheat limit, K
r_c	Radius of curvature, m
T	Temperature, K
t	Time, s
u	Velocity, m/s
x, y, z	Coordinate, m

Greek Symbols

δ_l	Wet wick thickness, m
ϵ	Porosity
ϵ_r	Emissivity
η	Efficiency
μ	Viscosity, Pa-s
σ	Surface tension, N/m
θ_c	Contact angle

Subscripts

a	Air
c	Capillary
$c - v$	Capillary-viscous
CHF	Critical heat flux
g	Gas
l	Liquid
lg	Liquid-gas
s	Solid, substrate
sh	Superheat
w	Wick, water

Superscript

*	Dimensionless
---	---------------

matrix, followed by debinding and sintering. However, making metallic sub-millimeter pores with 3D-printing has been a challenge, limiting permeability and capillary performance [14].

Using ceramics (oxides and monoxides), similar solid matrices have been fabricated [15] while allowing for sub-millimeter pores and solid matrices [16]. So, although using metals results in a larger effective wick thermal conductivity, 3D-printing with ceramics currently allows for finer, porous unit-cell structures including metasurfaces. Examples of ceramic-based porous applications have included ceramic wicks incorporating a bilayer evaporator [17], wicks fabricated by slip-casting

mullite and alumina slurry [18], and a sintered silicon carbide particle wick for use in loop heat pipes [19]. Ceramic wicks have also been studied for use in burning of liquid fuels, where the standing gaseous flame provides heat for evaporation on the wick surface [20].

In contrast to sintered metallic particle wicks, ceramic-based wicks have the benefit of inertness and, when appropriate, can help with the device reliability and maintenance. The heat load limit of an open-system evaporator, based on capillary rise against gravity (Fig. 1) is controlled by the wick's capillary-viscous or superheat (boiling) limit. For metallic wicks with small particles enhancing capillary pressure and large effective thermal conductivity, the heat load limit has been shown to be the capillary-viscous limit, where the capillary pressure in the wick is insufficient to maintain liquid replenishment. The ceramic wicks have a smaller effective thermal conductivity and may instead be limited by the wick superheat limit, where the onset of boiling forms bubbles and dry patches within the pores of the wick.

Here, a 3D-printed ceramic metasurface wick is designed and fabricated for efficient surface evaporation in an open-system evaporator. Unlike the laser powder bed fusion technology that has been used to manufacture wick structures from metal powders (which can restrict permeability and block pores), micro 3D-printing with ceramics allows for precise control of the structural parameters, under the constraint of a minimum resolution. This permits the design of unit-cell based wicks for optimal thermal performance. For example, a 3D-printed gyroidal unit-cell based wick was recently demonstrated in [21] for vapor chamber condensation. The two-dimensional lattices, i.e., 2-D Bravais lattices, are five lattices grouped into four lattice systems [22], namely, monoclinic, orthorhombic, tetragonal, and hexagonal. The hexagonal lattice is selected for its simplicity, adaptability, and low porosity. The monolayer wick is constructed using cylindrical struts, with the diameter of the struts and the spacing between them dictated by the fabrication size restrictions. This is referred to as the hexagonal-prism unit-cell wick (HPW).

Fig. 1 shows a schematic of the vertically-oriented ceramic hexagonal-prism unit-cell open-system evaporator wick, with a ceramic substrate, heat supply q to the substrate, liquid supply \dot{m}_l from the bottom, wet-wick-surface evaporation \dot{m}_{lg} , and temperature T_{lg} . The substrate-wick interface temperature T_{w-s} is also shown, along with the critical heat flux (CHF) limits discussed previously.

This work presents the first trial of this newly designed ceramic (alumina) 3D-printed wick structure for open-system evaporation, so the demonstration of its fabrication and evaporator performance are of primary importance. Here, the optimal unit-cell structure parameters (design) are assessed using 3-D numerical simulations, so the experimental investigation in this study is also focused on the validation of numerical simulations. The Surface Evolver (SE) code [23] is first used in order to predict the static liquid meniscus topology within the wicks. This program has previously been used to predict liquid capillary surfaces in wicking microstructures for a variety of unit-cell structures including spheres, ribs, and cylinders [24]. The static meniscus unit-cell can then be meshed and used in CFD software to predict the thermal characteristics (heat flow) of the microstructures [25], as well as for the liquid flow to determine the permeability [26]. The thermal conductance together with the permeability help to assess the overall wick performance.

2. 3D-printed, ceramic hexagonal-prism unit-cell wick and its effective properties by simulation

2.1. 3D-printed, ceramic hexagonal-prism wick

The evaporator wicks are designed for their optimal thermal-hydraulic performance. A wick figure of merit can be defined based on the maximum heat flux and thermal conductance [8], e.g., a dimensional product $q_{CHF}(G/A)$. The specific conductance G/A is the

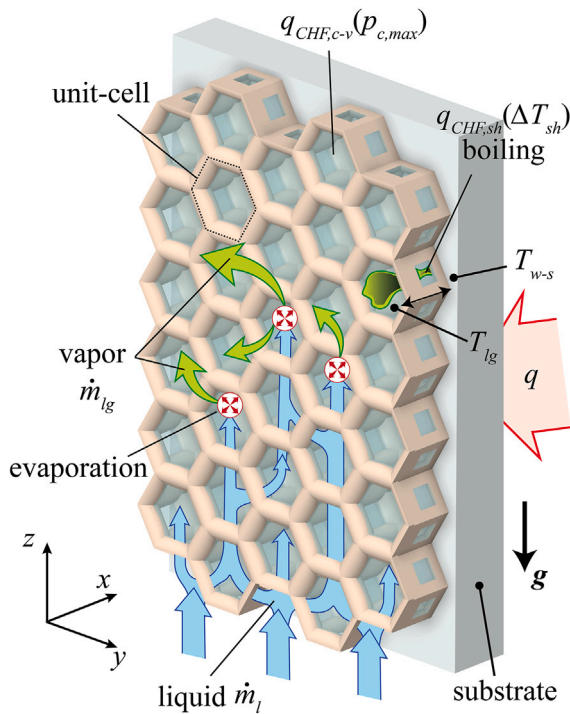


Fig. 1. A schematic of the operational 3D-printed, hexagonal-prism unit-cell evaporator wick. A heat flux q (red arrow) is applied to the substrate, causing evaporation (mass flux \dot{m}_{lg}) of the meniscus with a superheat temperature difference $\Delta T_{sh} = T_{w-s} - T_{lg}$. The meniscus recedes, pulling liquid by capillary action at mass flux \dot{m}_l (blue arrows) from a liquid reservoir against the gravity vector g . If the superheat temperature ΔT_{sh} becomes too large, the superheat limit ($q_{CHF,sh}$) is reached and boiling occurs, causing significant dry areas (bubbles) in the pores. Instead, if the capillary pressure is insufficient to pull liquid for evaporation at some position, then the capillary-viscous limit ($q_{CHF,c-v}$) is reached.

ratio of the wet wick effective thermal conductivity and wick thickness, $\langle k \rangle / \langle \delta_l \rangle$. The maximum or critical heat flux is controlled by the liquid and vapor supply/removal, governed by the capillary flow and viscous drag, called the capillary-viscous limit $q_{CHF,c-v}$, or by the so-called wick superheat limit $q_{CHF,sh} = (G/A)\Delta T_{sh}$, which is the onset of bubbles forming within the wick. $q_{CHF,c-v}$ is proportional to the maximum capillary pressure $p_{c,max}$ and the permeability K . Meanwhile, ΔT_{sh} is found experimentally. In [27], a superheat limit of around 15 K was found for a water-alumina structure.

The design is driven by the unit-cell structure and ceramic 3D-printing feature constraints. Starting with a 150 μm minimum feature dimension, a monolayer wick should have a good effective thermal conductivity, so struts of diameter 150 μm are grown perpendicular to the substrate. The distance between these struts is also kept to 150 μm . Next, the permeability and capillary pressure of the monolayer wick are considered. For good capillary pressure, the struts should be connected, allowing the receding meniscus to form a 3-D surface with large curvature (for example, a pin fin design, having no top lateral struts, leads to a smaller capillary pressure). Connecting the struts with similar lateral struts in a hexagonal lateral arrangement leads to the most controlled meniscus topology given reasonable capillary pressure and permeability. The unit-cell is shown in Fig. 2.

The portion of cell resting on the substrate uses half-cylinders, while the opposite side has full cylindrical struts. The side square window controls the permeability, while the top opening controls the capillary pressure. The porosity of the unit-cell is $\epsilon \approx 0.70$. In other applications, such as the flow-boiling canopy wick [9], multiple vertical layers may be desired. In this case, the top opening can employ half cylinders to

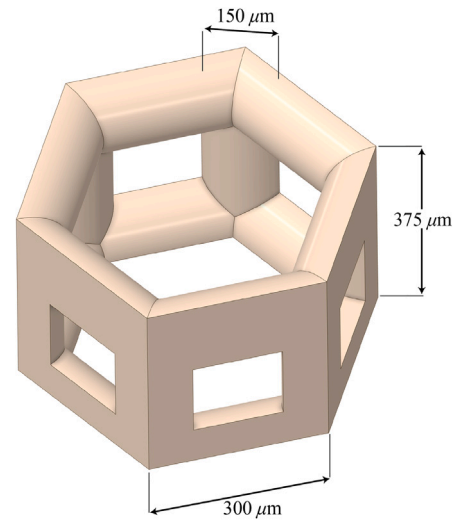


Fig. 2. Schematic of the hexagonal-prism unit-cell as simulated and replicated to create the full evaporator wick. The porosity of the unit-cell is $\epsilon \approx 0.70$.

form a 3-D unit-cell for vertical stacking, rather than the 2-D monolayer unit-cell.

A 10 mm \times 20 mm alumina evaporator wick based on this unit-cell is fabricated on a 1 mm substrate for an open-system evaporation experiment. The wick was printed by Boston Micro Fabrication with their the microArch S240 using micro stereolithography, which can provide up to 10 μm resolution [28]. The fabrication involves a sequential washing, debinding, and sintering of the alumina, starting with a slurry. Fig. 3 shows images of the fabricated evaporator wick, with (a) optical, and (b) scanning X-ray micrograph. The alumina surface is smooth and structural defects are rather absent.

2.2. Calculated capillary pressure

With increasing heat flux, more liquid evaporates from the liquid-vapor interface (meniscus) of the wick which is anchored to the solid structures at contact angle θ_c , requiring a greater capillary pressure to sustain liquid flow from the water reservoir to the wick for evaporation. As a result, the meniscus recedes deeper within the wick, increasing the capillary pressure by reducing the radius of curvature r_c of the meniscus. At even larger heat flux, the liquid-vapor interface can reach its maximum sustainable capillary pressure ($p_{c,max}$) before dryout.

The variation of the 3-D static, equilibrium meniscus topology in the hexagonal-prism wick with changing capillary pressure (including $p_{c,max}$) is predicted using the SE code [23]. In SE, the capillary surface and contacts with solid structures are established with geometrical constraints and meshed into faces, bounding the liquid volume (body). A dimensionless capillary pressure is prescribed as the boundary condition on the liquid body, and the SE code iteratively predicts the new meniscus topology by minimizing the surface energy using the gradient descent method.

Using symmetry, 1/6 of the wick unit-cell geometry with water is simulated, with the liquid anchored to the upper struts using an assumed contact angle $\theta_c = 45^\circ$ for the water-alumina contact. This contact angle was approximated due to the observed hydrophilic properties, and this is dependent on the 3D-printed sintered alumina particles and associated surface roughness. In [27,29], they report similar values of the contact angle for water-alumina, albeit with different types of porous structures. Various dimensionless capillary pressures p_c^* were prescribed in SE as boundary conditions on the liquid surface to observe the change in the average liquid thickness $\langle \delta_l \rangle$ inside the wick. For each case, the energy minimization is iterated until $\langle \delta_l \rangle$ is

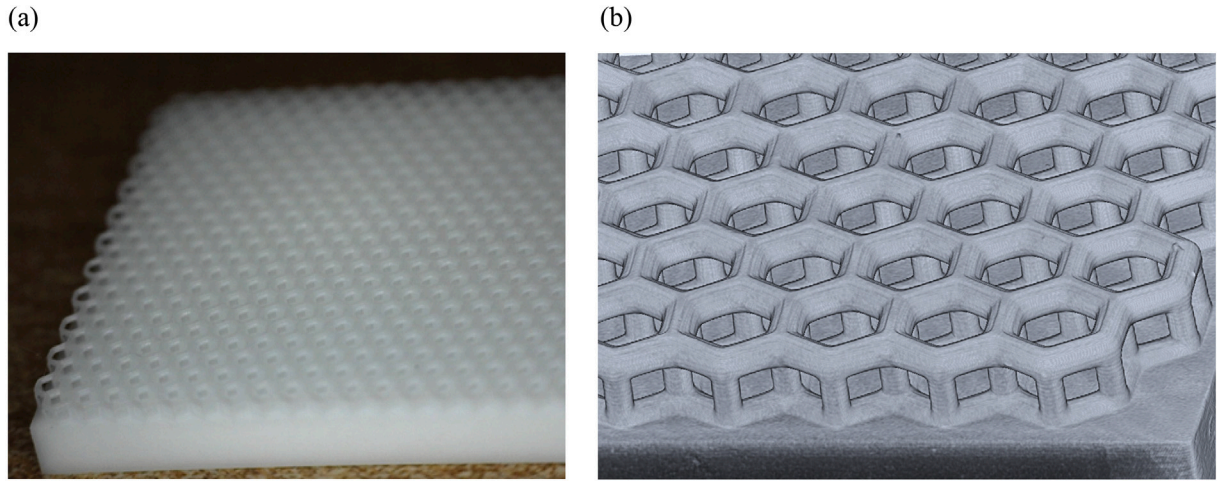


Fig. 3. (a) Optical image of the 3D-printed 10 mm × 20 mm alumina hexagonal-prism evaporator with a 1 mm substrate. (b) A close-up of the wick captured by scanning X-ray microscopy (SXM).

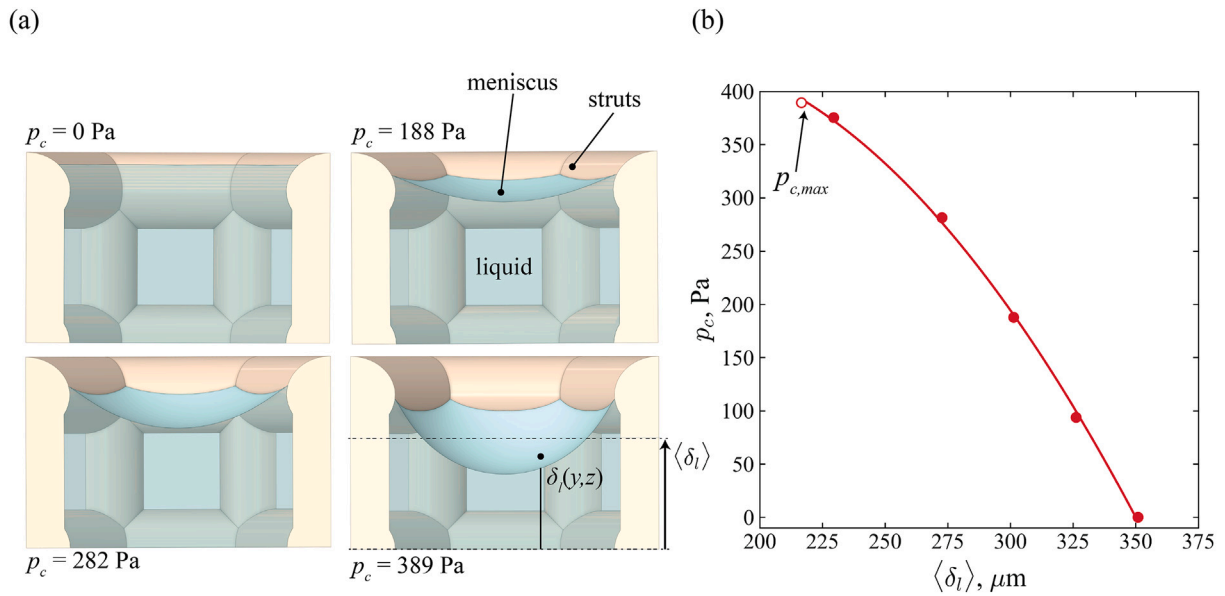


Fig. 4. (a) Cross section of the unit-cell wick showing the meniscus topology variations at selected capillary pressures, as predicted by SE. The local film thickness $\delta_l(y, z)$ and its surface-averaged thickness $\langle \delta_l \rangle$ are shown. (b) The variation of the predicted capillary pressure with the average meniscus thickness. The maximum capillary pressure ($p_{c,max}$) with a stable meniscus is also marked. The solid line is drawn to fit the data.

converged. Due to the small dimension, the gravity force is neglected in the SE simulations (the Bond number is small within each unit-cell). Using the relevant length scale, the dimensionless capillary pressure is converted to a dimensional one using [30,31]

$$p_c = \frac{p_c^* \sigma_{l-g} \cos \theta_c}{d_s}, \quad (1)$$

where d_s is the diameter of the struts (150 μm). The water surface tension used is $\sigma_{l-g} = 0.059$ N/m (corresponding to saturation temperature at 1 atm).

The SE simulation results (shown in Fig. 4) show the meniscus receding into the wick with increasing capillary pressure. The last stable meniscus was found when $p_c = 389$ Pa, and this point is indicated with an unfilled circle. Beyond this capillary pressure, the meniscus is no longer able to anchor to the upper struts, so this is considered the maximum capillary pressure of the wick ($p_{c,max} = 389$ Pa). Specifically, the meniscus contact line location attempts to jump into the side square window region, which makes the simulation unstable.

2.3. Calculated effective thermal conductivity and specific conductance

Using the finalized meniscus topology generated by SE, the 1/6 meniscus is exported by generating an STL file storing the vertex, edge, and face coordinates. The STL file (containing the 1/6 meniscus) is imported into ANSYS Spaceclaim and inserted to the solid structure (Fig. 2). Note that Fig. 4(a) is created after this step. After the liquid and solid domains are defined, the structures are then imported into ANSYS Meshing, where the entire volume is meshed with polyhedral elements with a maximum cell length of 2.5 μm , and the Shared Topology feature is used at the solid–liquid interfaces for conjugate heat transfer. For the thermal simulation, it was found that increasing the number of mesh cells from around 450 thousand to 800 thousand changed (increased) the predicted heat flow rate (q) by about only 1.5%, so the larger of the mesh sizes was selected for simulation.

The mesh is then imported into ANSYS Fluent and the thermal simulation is performed with a superheat temperature-difference boundary condition $T_{w-s} - T_{lg}$. The high temperature T_{w-s} is prescribed at the

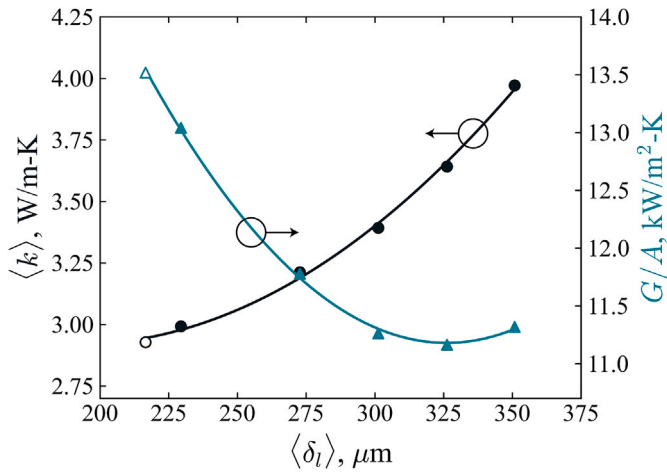


Fig. 5. Predicted effective thermal conductivity and specific conductance of the alumina hexagonal-prism unit-cell evaporator wick with respect to the wetted wick thickness (changing depending on the capillary pressure). The solid lines are drawn to fit the data.

substrate contact with the wet wick, while the meniscus is prescribed at the liquid-gas interface temperature T_{lg} . In this case T_{lg} was set to the saturation temperature, and the superheat temperature was 5 K (T_{w-s}, T_{lg} ; 378, 373 K). The vapor-exposed boundaries of the solid are assumed adiabatic, while the exterior sides (both solid and liquid) use the symmetry boundary condition. The thermal conductivity of alumina (Al_2O_3) is 32 W/m-K [32], and the value used for water (saturation temperature at 1 atm) is 0.68 W/m-K. The average heat flow through the substrate into the wick, $\langle q \rangle$, as well as the averaged wet wick thickness $\langle \delta_l \rangle$ predicted by SE, are used to calculate the local specific conductance and effective thermal conductivity of the evaporator wick as

$$G/A = \frac{\langle q \rangle}{T_{w-s} - T_{lg}}; \quad \langle k \rangle = \frac{\langle q \rangle \langle \delta_l \rangle}{T_{w-s} - T_{lg}}. \quad (2)$$

The results of the thermal simulations are presented in Fig. 5, where the calculated G/A and $\langle k \rangle$ of the unit-cell wick are shown. The unfilled scatter points indicate the data at $p_{c,max}$. The effective thermal conductivity increases monotonically with the wetted wick thickness $\langle \delta_l \rangle$. However, the predicted G/A reaches a minimum value near the equilibrium ($p_c = 0$ Pa) topology. As the liquid thickness $\langle \delta_l \rangle$ becomes larger, there is more surface area available for heat transfer (by evaporation) from the liquid-vapor interface (the meniscus has larger surface area) so G/A , proportional to the heat flow $\langle q \rangle$, increases. However, the volume of water (with low thermal conductivity) is also larger when $\langle \delta_l \rangle$ is large, decreasing G/A .

2.4. Calculated permeability

The permeability of the 3D-printed evaporator wick is predicted using CFD simulations, and is later used to estimate the capillary viscous limit $q_{CHF,c-v}$ of the wick. The permeability is controlled mainly by the dimensions of the square windows connecting adjacent unit-cells (Fig. 2), as well as the topology of the meniscus ($\langle \delta_l \rangle, p_c$) since this affects the cross-sectional area available for liquid flow (the meniscus topology is assumed static while the liquid flows below the surface). Finally, the permeability may not be isotropic and depends on the direction of flow. In the vertical orientation (Fig. 1) of the open-system evaporator experiment considered here, this flow is primarily in the z direction against gravity.

The unit-cell wick mesh is mirrored with symmetry in ANSYS Fluent in order to form the simplest rectangular unit-cell, such that there are two permeabilities K_y and K_z . For the liquid flow simulation,

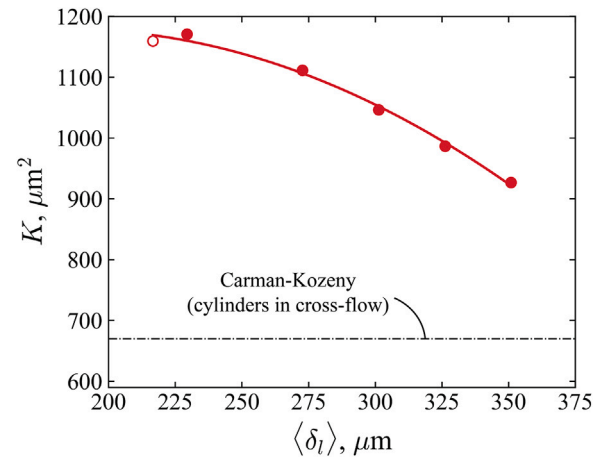


Fig. 6. CFD-predicted permeability of the hexagonal-prism unit-cell evaporator wick with respect to the meniscus thickness. An analytic calculation based on the Carman-Kozeny relation is also shown. The solid line is drawn to fit the data.

laminar incompressible flow is assumed. The interfaces with the solid are considered to be no-slip, and the meniscus surface is assumed to be shear-free. The inlet and outlet are periodic with each other, while a pressure gradient is applied between them for solution of the momentum equation. The corresponding volume-averaged velocity in direction i is used alongside the system dimension (unit-cell length L) to predict the permeability in direction i by the Darcy law which applies due to the small Reynolds number; the liquid velocities are on the order of mm/s,

$$K_i = \frac{\mu_l L}{\Delta p_i} u_{l,i}. \quad (3)$$

The CFD permeability predictions are shown in Fig. 6. The permeability appears to increase as the meniscus recedes into the wick. This effect is a result of the liquid-solid interfacial area (causing viscous drag) becoming smaller as the meniscus drops to the lower part of the upper struts (Fig. 4). It was found that the permeability in direction x and y had negligible difference, so a single (isotropic) permeability is shown in Fig. 6. The permeability of packed beds can also be estimated by the Carman-Kozeny relation [33]

$$K = \frac{\epsilon^3}{36k_K(1-\epsilon)^2} \left(\frac{3}{2} d_s \right)^2, \quad (4)$$

where d_s is the diameter of the struts and k_K is the Kozeny constant. Here, we approximate the ceramic wick as a staggered array of cylinders in cross flow with porosity $\epsilon = 0.70$. For this configuration, $k_K \approx 8$ [34]. The Carman-Kozeny relation result is shown alongside the CFD predictions, and as expected, gives a lower permeability. One reason is the hexagonal arrangement of the cylinders (missing central cylinder compared to the staggered arrangement). In addition, the flow does not pass over the top part of the upper struts, due to the free-shear meniscus present below it.

Fig. 7(a) and (b) are snapshots from the thermal and liquid flow simulations with the relevant boundary conditions, for the case of $p_c = 375$ Pa. The temperature distribution shows thermal non-equilibrium between the liquid and solid phases, with the meniscus surface at the liquid-vapor equilibrium temperature T_{lg} , and the wick-substrate temperature at T_{w-s} . The velocity distribution is governed by no-slip at the liquid-solid interface and zero shear at the liquid-gas (vapor) interface. The permeability is calculated from the prescribed pressure drop across the unit-cell and the resulting average liquid velocity.

3. Open-system evaporation experiment with ceramic wick

The performance of the fabricated ceramic wick was evaluated by measuring the rate of water evaporation. The experimental setup was

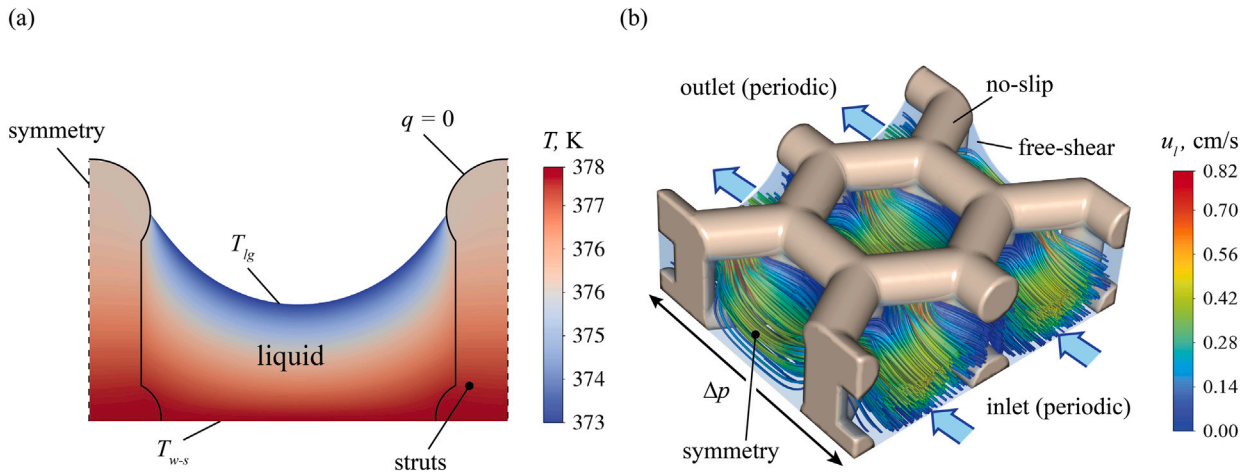


Fig. 7. Representative snapshots of (a) the temperature distribution across a section in the unit-cell from thermal simulations used to predict the effective thermal conductivity $\langle k \rangle$ and the specific conductance G/A of the hexagonal-prism evaporator wick, and (b) the flow streamlines and velocity distribution in the rectangular domain used to predict the permeability K . Both snapshots are for $p_c = 375$ Pa.

partially modified from that used for sintered copper-particle wicks in [3], and is shown in Fig. 8. Heat was supplied using a cartridge heater (CHA1152, Kashima, Japan). The applied voltage was controlled with a transformer (V-130-5, Yamabishi Denki, Japan). The cartridge heater was inserted into a copper heater block. This heater block was connected to a copper bus bar (8 mm \times 8 mm \times 42 mm) with a solder paste. Thermocouples were embedded into the copper bus bar to determine the heat flux. The linear regression provides the heat flux as

$$q = -k \frac{N \sum_i x_i T_i - \sum_i x_i \sum_i T_i}{N \sum_i x_i^2 - (\sum_i x_i)^2}, \quad (5)$$

where k is the thermal conductivity of copper, N is the number of data points, and x is the location of thermocouple along the copper bus bar.

The ceramic wick sample (10 mm \times 20 mm) was connected to the copper bus bar. We used Nano-Diamond Grease (TK-GR2, Sanwa Supply, Japan) as the thermal interface material (TIM), which has a thermal conductivity of 16 W/m-K. The thickness of the TIM was estimated to be 0.1 mm. The ceramic wick was held vertically with its bottom immersed in the water reservoir (57 mm \times 57 mm in the bottom area and 27.6 mm in height). The wick was partially submerged in the water reservoir, with an average submerged length of 5 mm. We used an underwater wick support to prevent the wick from sliding down due to gravity. This wick support was grounded outside the water reservoir so that a precise measurement of the water mass variation could be made with minimum disturbance. The variation in the water mass was measured using an electronic balance (AUW-120D, Shimadzu, Japan). We supplied water to the ceramic wick to easily initiate capillary transport of water from the water reservoir. We stepwise increased the voltage supplied to the cartridge heater. The water evaporation rate was determined in steady-state. The evaporation rate was calculated from the liquid loss (or added make-up water),

$$\dot{M}_{lg} = -\frac{dM_l}{dt}, \quad (6)$$

where M_l is the water mass in the water reservoir. The evaporation efficiency is defined as

$$\eta_e = \frac{\dot{M}_{lg} \Delta h_{lg}}{Q}, \quad (7)$$

where Q is the heat transfer rate. When the measured heat flow rate Q and the evaporation energy rate $\Delta h_{lg} \dot{M}_{lg}$ match, the evaporation efficiency is unity. Heat losses lead to a value smaller than unity.

An IR camera (Xi400, Optris, Germany) is used for surface thermometry, i.e., to detect and record the thermal radiation emission in the

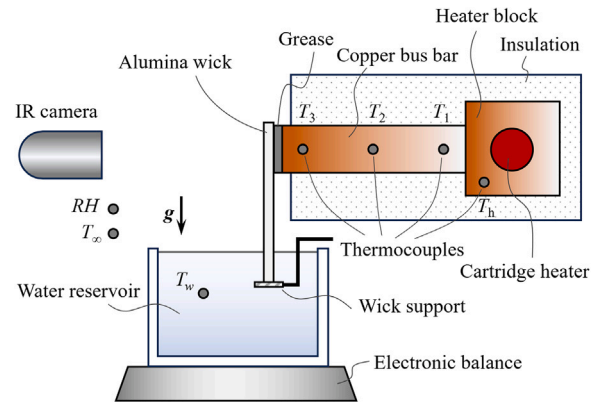


Fig. 8. Schematic of the experimental setup used for evaluating the water evaporation with the alumina wick (not to scale). The wick attachment has changed from the copper wick experiment described in [3].

wavelength range of 8–14 μm . The surface-average emissivity of the water-filled hexagonal-prism alumina wick is determined using area averaging

$$\langle \epsilon_r \rangle = (1 - A_l^*) \epsilon_{r,s} + A_l^* \epsilon_{r,l}, \quad (8)$$

where A_l^* is the liquid surface area fraction, $\epsilon_{r,s}$ is the alumina emissivity, and $\epsilon_{r,l}$ is the liquid emissivity. Considering the spectral radiative properties of water and alumina in the wavelength range of this measurement, we estimated $\langle \epsilon_r \rangle = 0.9$.

In evaluating the results, uncertainties in thermocouple temperature (± 0.5 $^\circ\text{C}$), thermocouple location (± 0.4 mm), and water mass (± 0.02 mg) are considered. The uncertainty propagation gives the heat flux uncertainty as

$$U_q^2 = \sum_i \left(\frac{\partial q}{\partial T_i} \right)^2 U_T^2 + \sum_i \left(\frac{\partial q}{\partial x_i} \right)^2 U_x^2. \quad (9)$$

For temperatures determined by IR measurement, uncertainty is estimated as ± 5 $^\circ\text{C}$, which corresponds to $\pm 2\%$ of the full scale of temperature range (i.e., 250 $^\circ\text{C}$), based on the specification of the IR camera.

The results are summarized in Fig. 9(a) and (b). The time variations of the heater, copper bus bar, air, and water reservoir temperatures, as well as the ambient relative humidity are shown. The temperatures increased with the electric potential applied to the cartridge heater, as

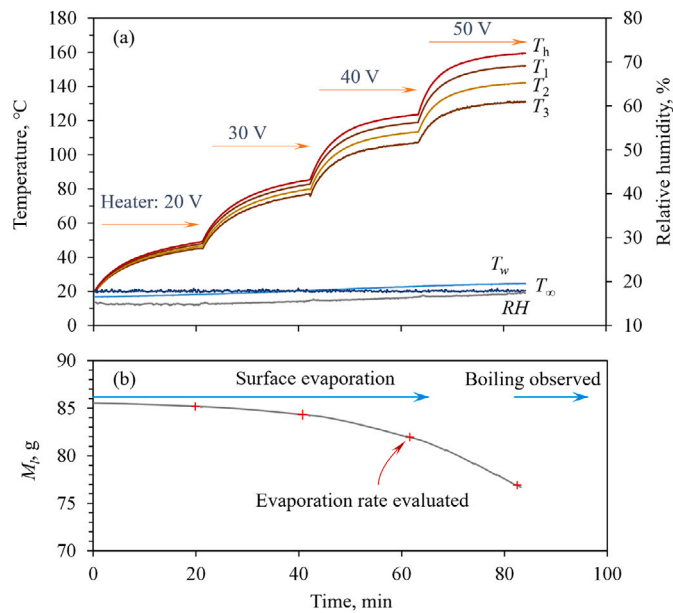


Fig. 9. (a) The measured time variations of the heater, copper bus bar, air, and water reservoir temperatures, as well as the relative humidity. The heater applied electric field was increased in increments of 10 V. For the 50 V data, some bubble formation and droplet ejection was observed. (b) Time variation of the measured mass in the liquid reservoir; at the marked elapsed times, the rate of water mass loss was determined.

shown in Fig. 9(a). As indicated with the water mass reduction in Fig. 9(b), we observed boiling at high heat load (occurring in the upper portion of the wick). The results for applied electric potential of 20, 30, 40 and 50 V are used. At the applied electric potential of 50 V, bubbles began to appear and droplets were ejected, so the superheat limit was reached. The complete experimental data are presented later in Section 6.

4. Simulation of heat transfer in open-system evaporation test

Numerical simulations are used to further analyze the performance of the fabricated and tested ceramic wick; namely, a prediction of the wick-substrate interface temperature is desired in order to estimate the superheat temperature ΔT_{sh} . The wick-substrate interface temperature could not be measured in the experiment since thermocouples could not be placed there. The geometry and materials from the experiment (Fig. 9) are replicated in ANSYS Fluent. This includes the rectangular (10 mm \times 15 mm) ceramic wick, where the 5 mm submerged region is not simulated, and the ceramic substrate connected to the 8 mm \times 8 mm copper bus bar with the TIM paste, up to the thermocouple position at T_3 . The wetted wick is treated as a solid material (conduction simulation) with the same effective thermal conductivity as predicted in the unit-cell wick thermal simulation (Fig. 5), using $\langle \delta_i \rangle$ as the material thickness. We use the value of $\langle k \rangle = 3.64$ W/m-K, corresponding to $p_c = 86$ Pa, since this is close to the capillary pressure required to pull the water from the reservoir, against gravity, into the region in contact with the bus bar for evaporation.

At the surface with temperature T_3 , the heat flux q based on Q/A for a given voltage of the experiment is imposed as the boundary condition there. Here, we approximate the evaporation surface temperature T_{lg} to be uniform across the surface of the wick, and the other surfaces (facing the z and y directions) to be adiabatic. The energy equation is initially solved for the wick, substrate, TIM, and copper bus bar using an estimate for T_{lg} based on a simple, analytic 1-D thermal resistance model. Due to the fin effect in the lower part of the wick structure (which is not connected to the bus bar), the corresponding T_3 does not match the experimentally obtained value. So, T_{lg} is updated in order to

converge T_3 . The converged 3-D numerical predictions demonstrate the fin effect in the lower part of the wick which affects the non-uniform temperature at the interface of the substrate and the wick (T_{w-s}).

An example of the 3-D numerical results is shown in Fig. 10 for a heater electric potential of 40 V. Fig. 10(a) compares the numerical axial temperature variations (direction x in Fig. 1) with the available experimental measurements. The numerical prediction of the wick surface temperature T_{lg} shows excellent agreement with the IR temperature measurement there. Meanwhile, the lowering of the substrate temperature due to the fin effect is illustrated with comparison to the 1-D analytic thermal resistance prediction where the change in cross-sectional area due to the wick is not considered. The fin effect results in temperature non-uniformity at the wick-substrate interface; thus, an average temperature (across the entire 10 mm \times 15 mm area) is used in the predictions, as shown in Fig. 10(b) and (c). The complete numerical results for all the test cases is presented later in Table 1 (Section 6), alongside comparison to all of the experimental measurements.

5. Sintered-copper-particle monolayer wick effective properties by simulation

The effective properties of the sintered copper particle monolayer wick fabricated and tested in our previous work [3] are predicted by the same methodology described in Section 2. These include capillary pressure, thermal conductance, and permeability. The performance of the ceramic and copper monolayer wick for open-system evaporation can then be compared. The copper particles in the wick have an average diameter of 78 μ m, and they are sintered with the substrate surface. The spherical particles, when randomly packed, have a bulk porosity around $\epsilon = 0.40$. A single particle layer on a planar substrate and under a close-packed arrangement has a similar porosity. This is significantly smaller than the hexagonal prism wick, thus improving the effective thermal conductivity.

The simulation domain is constructed first in SE. Since a hexagonal (close-packed) arrangement is considered, then using symmetry the simulated geometry involves a single spherical particle surrounded by a small liquid meniscus of hexagonal outer dimension. Sintering of the particles with the substrate is considered by cutting the particle with a horizontal plane, such that the height of the particle is $d_p/8$ where d_p is the particle diameter (78 μ m), which shows general agreement with SEM side-profile images of the sintered particle monolayer.

Following the procedure outlined in Section 2, the meniscus topology of the monolayer wick is predicted by surface energy minimization in SE. The resulting meniscus topologies in the unit-cell are imported into ANSYS Fluent for the thermal and fluid simulations. The effective wick properties of the sintered copper-particle monolayer are summarized in Fig. 11. Fig. 12 shows an SEM image and the corresponding modeling domain used in the simulations for the sintered-copper-particle monolayer wick tested in [3]. In addition, the receding meniscus SE results are shown along with snapshots of the thermal and fluid simulations used to predict the wick properties.

As expected, the predicted maximum capillary pressure $p_{c,max} = 8560$ Pa for the sintered-particle wick is significantly higher than that of the 3-D printed ceramic wick by about 20 folds. The predicted thermal conductivity and conductance are also larger, $\langle k \rangle$ by nearly 2 folds, and G/A by about 10 folds) owing to the lower porosity and higher solid thermal conductivity of the sintered copper particle wick. However, the sintered particle wick has a significantly smaller predicted permeability (200 folds smaller). As discussed later, these differences have significant effect on the performance metrics of the wick, including the dryout limits.

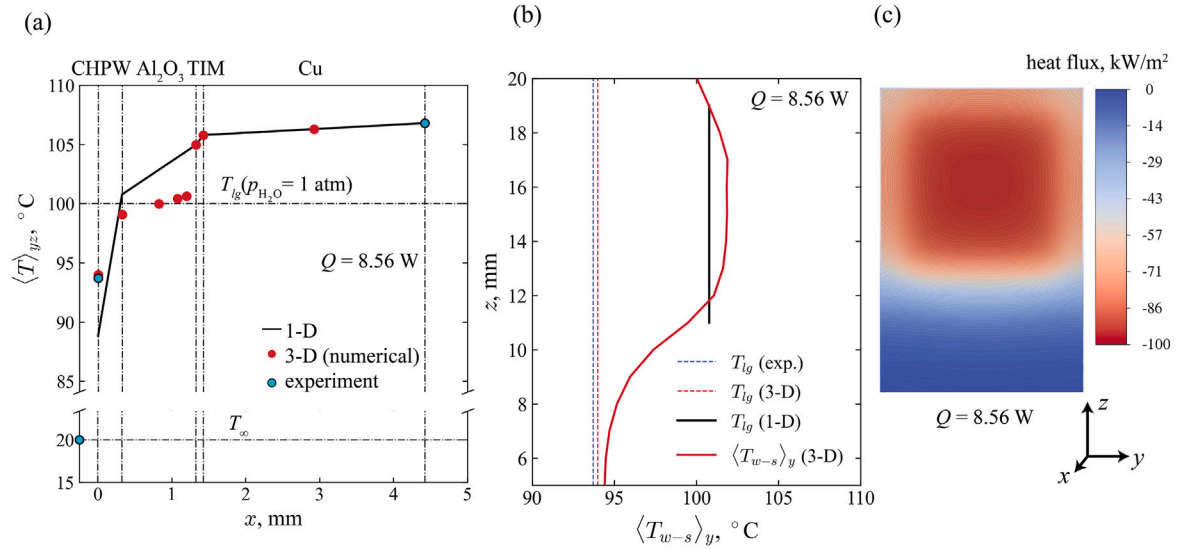


Fig. 10. (a) Axial variation of the lateral-averaged temperatures in the open-system evaporation test, including a 1-D analytic thermal resistance prediction, 3-D numerical predictions (capturing the fin effect), and experimental IR measurements (for the 40 V electric potential case). (b) The variation in y -averaged temperature with vertical position z at the wick-substrate interface by 3-D numerical simulation. (c) Predicted heat flux distribution on the wick surface (with uniform temperature T_{lg}) showing that a majority of the heat flow is in the region in contact with the bus bar. The simulation results are for the top 15 mm of the wick, where $z = 0$ corresponds to the bottom of the wick (submerged).

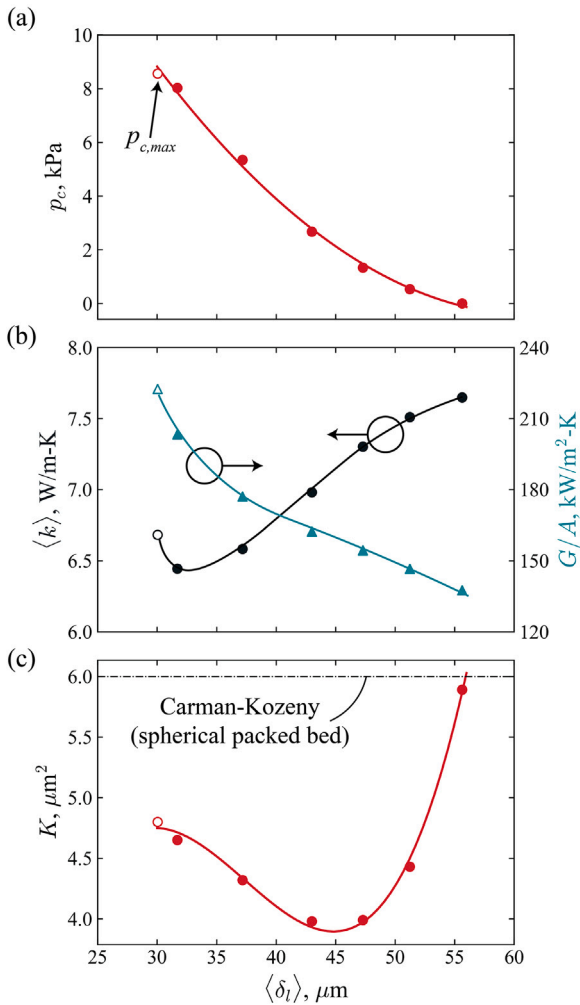


Fig. 11. Variations of the predicted (a) capillary pressure, (b) effective thermal conductivity and conductance, and (c), permeability including comparison with the Carman-Kozeny relation. The results are for sintered copper particles (78 μm particle diameter) with water as the liquid. The solid lines are drawn to fit the data.

6. Comparison of predicted and measured wick evaporation performance

In Table 1, the detailed experimental data for the open-system ceramic wick test is presented, including the estimated heat flow Q , thermocouple temperature measurement T_3 , the IR temperature measurements at the surface of the wick T_{lg} , and the evaporation efficiency η_e . The heat flow Q is estimated based on the temperatures measured in the copper bus bar (T_1 , T_2 , and T_3) along with the contact heating area, as discussed in Section 3. The data from the CFD wick property predictions and the open-system numerical simulation are also presented in the prediction columns (see Section 4). In this test, for the case of 50 V, a weak sizzling sound was observed, indicating the onset of boiling. With further increase in the electric potential, intense boiling with surface bubbles and water ejection were observed. We note that the measured water loss rate \dot{M}_{lg} is lower than what is expected from the estimated heat flow rate Q . This can be due to uncertainty/accuracy of the measured minute water mass loss rate and heat losses.

Between 20–40 V, the numerically-predicted evaporation surface temperatures T_{lg} show good agreement (despite the unintentional heat losses in experiment) with the IR surface temperature measurement (using surface emissivity $\epsilon_r = 0.9$). At the superheat case of 50 V, the agreement is poor, possibly due to the boiling condition being reached and the associated effects such as dry pores in the wick. Some of the wick properties can be directly estimated from the experiment and compared with the numerical predictions in Section 2. As an estimate of the effective thermal conductivity, we multiply the heat flow equations [Eq. (2)] with the evaporation efficiency η_e , using the total thermal resistance of the copper bus bar, the TIM, and the alumina substrate. Then we obtain $G/A = 11.7 \text{ kW/m}^2\text{-K}$ for the case of 40 V. Assuming the average meniscus thickness $\langle \delta_l \rangle = 300 \mu m$ (smaller than the wick thickness, due to receding meniscus during evaporation), we have $\langle k \rangle = 3.5 \text{ W/m-K}$. This result supports the validity of predicted effective thermal conductivity shown in Fig. 5. Directly measuring the wick permeability from the experimental results is challenging for this open-system configuration; however, we note that the porosity value we report (0.70) is fairly accurate, because as validated by optical images of the wick, the 3D-printing with ceramics allows for high-precision resolution on the features.

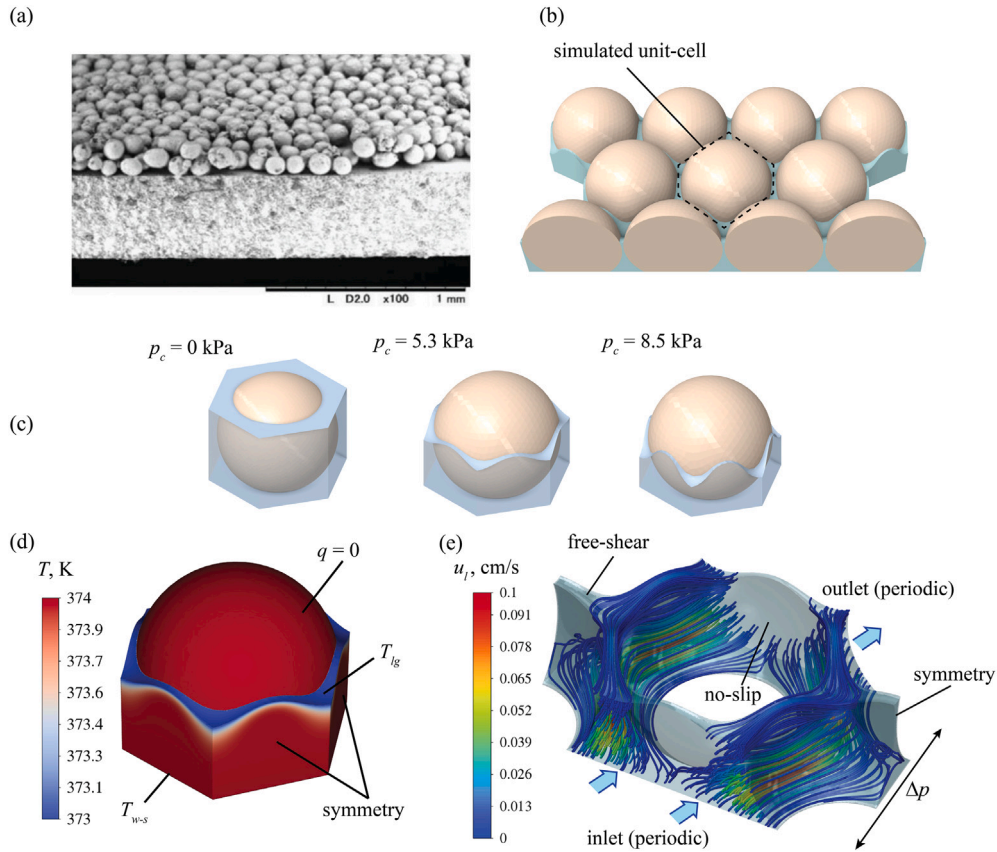


Fig. 12. (a) A SEM image of the 78 μm diameter sintered-copper-particle monolayer wick, used in the experiment of [3] (adapted from [3]). (b) Modeling domain visualization constructed from several of the simulation unit-cells designed in SE. (c) Meniscus topology variations at three capillary pressures, as predicted by SE. (d) Temperature distribution in the unit-cell from the thermal simulations. (e) Flow streamlines and velocity distribution within the rectangular domain used for the permeability predictions. Snapshots (d) and (e) are both for the case $p_c = 5.3$ kPa.

Table 1

Experimental results from the open-system evaporation test, also including the 3-D open-system temperature predictions which are based on the measured T_3 and Q .

Measured							Predicted (3-D)	
Heater, V	Q , W	q , kW/m ²	T_3 , °C	T_{lg} , °C	\dot{M}_{lg} , mg/s	η_e	$\langle T_{w-s} \rangle$, °C	T_{lg} , °C
20	1.77	27.7	45.3	43.5	0.353	0.480	43.7	42.7
30	4.03	63.0	77.0	72.4	0.915	0.530	73.4	71.0
40	8.56	133.8	106.8	93.7	2.478	0.662	99.1	94.0
50	14.86	232.2	130.9	99.1	5.043	0.768	117.5	108.7

6.1. Capillary-viscous limit

The capillary-viscous heat flux limit $q_{CHF,c-v}$ of the wicks can be estimated using the experimental conditions of the open-system evaporators, for both the ceramic wick and copper monolayer wick of [3]. In the capillary-viscous limit, the maximum capillary pressure difference ($p_{c,max}$) (pulling liquid from the reservoir) is equal to the viscous pressure drop by the Darcy law [Eq. (4)]. In this experiment, the liquid is pulled through a wicking length L_e in the z direction (Fig. 1) and wick cross-sectional flow area A_w , which is the product of the wick width and liquid thickness. Due to the vertical orientation, the gravitational pressure loss works against the capillary suction. Also, starting with a liquid velocity $u_{l,o}$ at the bottom of the wick, this velocity decreases along z and vanishes at the top location L_e due to evaporation. So, the average velocity is $u_{l,o}/2$, and we adjust the wicking height to $L_e/2$. Then the momentum conservation leads to

$$\frac{2p_{c,max}}{L_e} - \rho_l g = \frac{\mu_l}{K} u_{l,o} = \frac{\mu_l}{K} \frac{\dot{M}_{lg,c-v}}{\rho_l A_w}, \quad (10)$$

where $\dot{M}_{lg,c-v}$ is the maximum evaporation mass flow rate (or the maximum liquid flowing into the wick $\dot{M}_{l,c-v}$). Considering the effective area for evaporation A_e and the heat of evaporation gives the expression for the capillary-viscous limit heat flux as

$$q_{CHF,c-v} = \left(\frac{2p_{c,max}}{L_e} - \rho_l g \right) \frac{\Delta h_{lg} \rho_l K}{\mu_l} \frac{A_w}{A_e}. \quad (11)$$

For the ceramic wick, the wick properties predicted at $p_{c,max}$ are used for $q_{CHF,c-v}$ (Section 2), while the value for the copper particle wick is from [3]. The capillary-viscous limits of the wicks are presented in the next subsection.

6.2. Heat flux and superheat comparison

In Fig. 13, the experimental results for q are shown. The associated experimental uncertainty is also shown, based on the error propagation explained in Section 3. The superheat temperature $\Delta T_{sh} = \langle T_{w-s} \rangle - T_{lg}$ is determined using the 3-D numerical predictions as shown in Table 1. In this experiment, the superheat limit was reached at the 50 V case. The corresponding $q_{CHF,sh}$ is 232 kW/m², and this is shown with the horizontal and vertical dashed black lines. This is significantly smaller

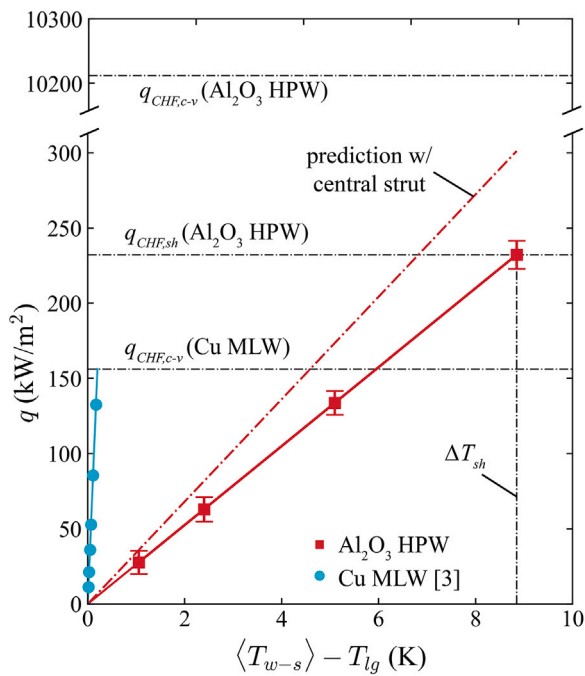


Fig. 13. Variations of the average heat flux q with the wick superheat. The experimental heat flux is used along with the predicted wick superheat for the ceramic 3D-printed wick (labeled HPW). The estimated uncertainty in the measured heat flux is shown with error bars. The highest heat flux resulted in formation of bubbles within the wick, so it is marked as the wick superheat limit (ΔT_{sh}). The broken red line is the open-system prediction with improved wick thermal conductivity by adding a central strut to lower the porosity. The predicted ceramic wick capillary-viscous heat flux limit is also shown. The previous experimental results with the copper wick are shown along with this wick's predicted capillary-viscous limit (labeled MLW).

then the capillary-viscous limit $q_{CHF,c-v}$ predicted by Eq. (11) which is near 10 MW/m^2 .

The copper-particle monolayer wick was recently demonstrated as a useful open-system evaporator, but it exhibited the capillary-viscous limit at high heat loads [3]. It was also shown that this capillary-viscous limit appeared even when the copper-particle size in the monolayer was changed (i.e., the average diameters of 78, 100, and 130 μm). These results are shown in Fig. 13 for a particle diameter of 78 μm . In contrast, the hexagonal-prism unit-cell wick overcomes this limit due to the wick's larger permeability enabled by the 3-D micro-fabrication, resulting in a higher maximum heat flux than this copper monolayer open-system evaporator. In this respect, the ceramic hexagonal prism unit-cell wick is superior to the copper monolayer wick. For reference, these dryout limits are illustrated in Fig. 1.

The experimental results show that the wick superheat limit, controlled by the effective thermal conductivity, dominates over the capillary-viscous limit. This suggests that improvement in its evaporation performance can be achieved by reducing the porosity of the structure. This is investigated numerically by incorporating a 150 μm central cylindrical strut to the original structure, reducing the porosity from about 0.70 to 0.60, while keeping the minimum feature dimension the same (for fabrication constraints). In this example, the strut is topped with a hemispherical cap. The corresponding increase in the effective thermal conductivity of the wick is predicted using the SE and thermal simulations, as shown in Fig. 14. For a case at $p_c = 94 \text{ Pa}$, the thermal conductivity increased by about 35% to $\langle k \rangle = 4.9 \text{ W/m-K}$. The predicted improvement in the heat flow of with this configuration is added to Fig. 13 as the broken red line. These second-generation design and fabrication considerations can be explored further in future studies.

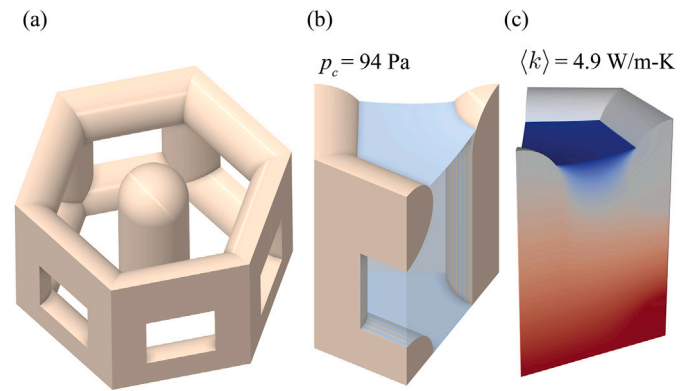


Fig. 14. (a) Ceramic hexagonal prism wick unit-cell with a central strut added to lower the porosity and increase the wet wick effective thermal conductivity (k). (b) SE-evaluated meniscus topology for $p_c = 94 \text{ Pa}$. (c) Temperature distribution with 5 K superheat used for the effective thermal conductivity prediction. Note that 1/6 of the geometry is simulated using symmetry.

7. Conclusions

3D-printing (additive manufacturing) allows for exploring the design of porous metasurfaces (unit-cell based surface structures) for control of the liquid-vapor phase change, surface temperature, and thermal-hydraulic transport. The traditional sintered metallic powder wicks allow for the particle size to dominate the capillary pressure through the interparticle pore spacing. So far, 3D-printing of metal powders has not led to successful control of the sintering and the pore spacing. However, ceramic microfabrication does currently allow for forming fine structures using particle-laden slurries and lithography. The binder is later removed and the remaining powder-based structure is sintered to up to a high density through a thermal process.

Using a minimum structural feature dimension of 150 μm , a single-layer hexagonal-prism unit-cell wick is designed with cylindrical struts which create square lateral liquid passages (affecting the permeability) and allow for a meniscus to form in the open hexagonal plane (affecting the capillary pressure). The struts control the effective thermal conductivity. The capillary pressure, permeability, and the effective thermal conductivity are predicted using 3-D numerical simulations, which can allow for the liquid meniscus to recede into the wick to create the maximum capillary pressure.

The designed hexagonal-prism unit-cell wick is fabricated by Boston Micro Fabrication using their microArch S240 printer that is based on projection micro stereolithography technology, achieving 10 μm resolution and 25 μm tolerance. The wick is 375 μm thick with a porosity of 0.70 and we predict a maximum capillary pressure of around 400 Pa and permeability of about 10^{-9} m^2 . The water-filled ceramic wick has a specific conductance around $10 \text{ kW/m}^2\text{-K}$, which is about a factor of 10 lower than that of the 78 μm sintered copper powder monolayer wick. However, the ceramic wick combination of maximum capillary pressure, permeability, and thickness results in its larger capillary-viscous heat flux limit $q_{CHF,c-v}$.

In an open-system evaporation test, the ceramic wick was tested, including wick surface temperature measurement by IR thermometry. 3-D numerical simulations are also performed confirming the experimental results. The experiment reached the wick's superheat limit (sizzling and water ejection from the wick was observed) $q_{CHF,sh}$, which is much lower than its high $q_{CHF,c-v}$. However, it outperforms the copper monolayer in a similar open-system experiment. The specific thermal conductance of the exploratory 3-D printed hexagonal-prism ceramic wick demonstrated here could be further improved in future designs by decreasing the porosity while keeping the fabrication-feature constraints. An example is shown in Fig. 14, where a central strut is added. This reduces porosity to 0.6, and the CFD results for a typical

meniscus topology determined by SE, shown also in Fig. 14, predict an effective thermal conductivity of 4.9 W/m-K. This would improve $q_{CHF,sh}$, as shown with a broken red line in Fig. 13.

CRediT authorship contribution statement

Lorenzo Franceschetti: Writing – review & editing, Writing – original draft, Visualization, Validation, Software, Investigation, Data curation, Conceptualization. **Yuki Kameya:** Writing – review & editing, Writing – original draft, Visualization, Validation, Supervision, Resources, Project administration, Methodology, Investigation, Funding acquisition, Formal analysis, Data curation, Conceptualization. **Mas-soud Kaviani:** Writing – review & editing, Writing – original draft, Resources, Project administration, Methodology, Funding acquisition, Conceptualization.

Declaration of competing interest

The authors declare that they have no known competing financial interests or personal relationships that could have appeared to influence the work reported in this paper.

Acknowledgments

We are grateful to Boston Micro Fabrication, Jason Bassi, for supporting sample fabrication of the polymer and alumina hexagonal prism wicks and the University of Michigan Center for Materials Characterization, Nancy Senabulya Muyanja, for X-ray microscopy. Y.K. is thankful for financial support from Japan Society for the Promotion of Science (JSPS KAKENHI Grant Number 23KK0271) and assistance in the experiment from Koya Ishiwata and Kei Nagatsuka at Chiba Institute of Technology. M.K. is thankful for insightful discussion on ceramic wicks with M.R. (Oveys) Shaeri (Advanced Cooling Technologies). L.F. is grateful for the National Science Foundation Graduate Fellowship support (Grant Number DGE 2241144).

Data availability

Data will be made available on request.

References

- [1] S.S. Bukhari, Y. Vardaxoglou, W. Whittow, A metasurfaces review: Definitions and applications, *Appl. Sci.* 9 (13) (2019) 2727.
- [2] M. Specht, M. Berwind, C. Eberl, Adaptive wettability of a programmable metasurface, *Adv. Eng. Mater.* 23 (2021) 2001037.
- [3] Y. Kameya, Y. Takahashi, M. Kaviani, Surface evaporation enhancement using porous metasurfaces: 3-D multiscale, open-system wick evaporators, *Int. J. Heat Mass Transfer* 216 (2023) 124605.
- [4] J. Ferreira, B. Furst, T. Daimaru, E. Sunada, M. Kaviani, Analytic characterization and operational limits of a hybrid two-phase mechanically pumped fluid loop based on the capillary pumped loop, *Int. J. Heat Mass Transfer* 183 (2022) 122019.
- [5] S.G. Liter, M. Kaviani, Pool-boiling CHF enhancement by modulated porous-layer coating: theory and experiment, *Int. J. Heat Mass Transfer* 44 (2001) 4287–4311.
- [6] G. Hwang, M. Kaviani, W. Anderson, J. Zuo, Modulated wick heat pipe, *Int. J. Heat Mass Transfer* 50 (2007) 1420–1434.
- [7] G. Hwang, Y. Nam, E. Fleming, P. Dussinger, Y. Ju, M. Kaviani, Multi-artery heat pipe spreader: Experiment, *Int. J. Heat Mass Transfer* 53 (2010) 2662–2669.
- [8] M. Kim, M. Kaviani, Multi-artery heat-pipe spreader: monolayer-wick receding meniscus transitions and optimal performance, *Int. J. Heat Mass Transfer* 112 (2017) 343–353.
- [9] M. Kim, M. Kaviani, Flow-boiling canopy wick for extreme heat transfer, *Int. J. Heat Mass Transfer* 117 (2018) 1158–1168.
- [10] P. Tao, G. Ni, C. Song, W. Shang, J. Wu, J. Zhu, G. Chen, T. Deng, Solar-driven interfacial evaporation, *Nat. Energy* 3 (2018) 1031–1041.
- [11] D. Jafari, W.W. Wits, B.J. Geurts, Metal 3D-printed wick structures for heat pipe application: Capillary performance analysis, *Appl. Therm. Eng.* 143 (2018) 403–414.
- [12] Z. Hu, D. Wang, J. Xu, L. Zhang, Development of a loop heat pipe with the 3D printed stainless steel wick in the application of thermal management, *Int. J. Heat Mass Transfer* 161 (2020) 120258.
- [13] H. Zhang, X.W.Z. Shi, F. Han, Compressive and energy absorption properties of pyramidal lattice structures by various preparation methods, *Materials* 14 (21) (2021) 6484.
- [14] X. Peng, G. Hang, H. Chen, Q. Duan, K. Huang, Super capillary performance of hybrid-structured wicks additively manufactured via laser powder bed fusion, *Addit. Manuf.* 99 (2025) 104653.
- [15] F. Zhang, Z. Li, M. Xu, S. Wang, N. Li, J. Yang, A review of 3D printed porous ceramics, *J. Eur. Ceram. Soc.* 42 (2022) 3351–3373.
- [16] J. Sun, D. Ye, J. Zou, X. Chen, Y. Wang, J. Yuan, H. Liang, H. Qu, J. Binner, J. Bai, A review on additive manufacturing of ceramic matrix composites, *J. Mater. Sci. Technol.* 138 (2023) 1–16.
- [17] R. Boubaker, Y. Lorgouilloux, S. Ouenzerfi, S. Harmand, Experimental study of a bilayer ceramic wick for the evaporator of a two-phase heat transfer device, *Int. J. Heat Mass Transfer* 228 (2024) 125609.
- [18] L. Berti, P. Santos, E. Bazzo, R. Janssen, D. Hotza, C. Rambo, Evaluation of permeability of ceramic wick structures for two phase heat transfer devices, *Appl. Therm. Eng.* 31 (2011) 1076–1081.
- [19] P. Yang, T. Yang, T. Gao, S. Zhao, J. Liu, P. Zhang, Experimental study on a dual compensation chamber loop heat pipe with a ceramic wick, *Appl. Therm. Eng.* 230 (2023) 120750.
- [20] Y.-X. Tao, M. Kaviani, Burning rate of liquid supplied through a wick, *Combust. Flame* 86 (1991) 47–61.
- [21] Z. Gu, K. Yang, H. Liu, X. Zhou, H. Xu, L. Zhang, Enhancing heat transfer performance of aluminum-based vapor chamber with a novel bionic wick structure fabricated using additive manufacturing, *Appl. Therm. Eng.* 247 (2024) 123076.
- [22] C. Kittel, *Introduction to Solid State Physics*, eighth ed., John Wiley and Sons, 2004.
- [23] K.A. Brakke, The surface evolver, *Exp. Math.* 1 (1992) 2.
- [24] R. Ranjan, J.Y. Murthy, S.V. Garimella, Analysis of the wicking and thin-film evaporation characteristics of microstructures, *ASME J. Heat Transf.* 131 (10) (2009) 101001.
- [25] R. Ranjan, J.Y. Murthy, S.V. Garimella, A microscale model for thin-film evaporation in capillary wick structures, *Int. J. Heat Mass Transfer* 54 (2011) 169–179.
- [26] R. Ranjan, A. Patel, S.V. Garimella, J.Y. Murthy, Wicking and thermal characteristics of micropillared structures for use in passive heat spreaders, *Int. J. Heat Mass Transfer* 55 (2012) 586–596.
- [27] E.C. Forrest, S.M. Don, L.-W. Hu, J. Buongiorno, T.J. McKrell, Effect of surface oxidation on the onset of nucleate boiling in a materials test reactor coolant channel, *J. Nucl. Eng. Radiat. Sci.* 2 (2016) 021001.
- [28] microArch 3D Printers, Boston Micro Fabrication, 2024, URL <https://bmf3d.com/10%CE%BCm-series-printers/>.
- [29] H. Leese, V. Bhurtun, K.P. Lee, D. Mattia, Wetting behaviour of hydrophilic and hydrophobic nanostructured porous anodic alumina, *Colloids Surfaces A: Physicochem. Eng. Asp.* 420 (2013) 53–58.
- [30] S. Modak, M. Kaviani, S. Hoenig, R. Bonner, Numerical analysis of meniscus dynamics in monolayer-wick dropwise condensation, *Numer. Heat Transf. A: Appl.* 76 (5) (1992) 301–322.
- [31] T.K. Kim, J. Ferreira, H. Jo, M. Kaviani, Flow-boiling canopy wick capillary-viscous limit, *Int. J. Heat Mass Transfer* 181 (2021) 121999.
- [32] AL (Alumina) Ceramic Data Sheet, Boston Micro Fabrication, 2024, URL <https://bmf3d.com/micro-3d-printing-materials>.
- [33] P. Carman, *Flow of Gases Through Porous Media*, Butterworth, 1956.
- [34] M. Sahaoui, M. Kaviani, Slip and no-slip boundary conditions at interface of porous, plain media, *Int. J. Heat Mass Transfer* 35 (1992) 927–943.